# Making kriging consistent with flow equations: application of Kriging with Numerical Covariances for estimating a contamination plume

Chantal de Fouquet, Mathieu Le Coz, Xavier Freulon, Lea Pannecoucke

Hydrogeology Journal

# Making kriging consistent with flow equations: application of Kriging with Numerical Covariances for estimating a contamination plume

--Manuscript Draft--

| | |
|---|---|
| **Manuscript Number:** | HYJO-D-22-00436R3 |
| **Full Title:** | Making kriging consistent with flow equations: application of Kriging with Numerical Covariances for estimating a contamination plume |
| **Article Type:** | Paper |
| **Funding Information:** | ANDRA — Not applicable<br>Programme d'investissements d'avenir — Not applicable |
| **Abstract:** | When the data are few, kriging hydraulic head or concentration with usual variogram models can lead to physically inconsistent results, because the non-stationarity induced by the flow or transport equations is not taken into account properly. Several methods have been proposed to account for these equations in the geostatistical estimation. A recent and general approach consists in incorporating them through specific covariance models. A set of random fields sampling uncertain parameters (e.g. conductivity) is first used as input of a flow simulator. Empirical “numerical” spatial covariances are then calculated between pairs of points  and  for the variable of interest (e.g. hydraulic head, concentration) on the corresponding set of flow simulator outputs. These non-stationary “numerical” covariances are consistent with the specific spatial variability of hydraulic head or concentrations. They are used in the estimation. In this paper, flow-and-transport simulations are thus combined with kriging to estimate contaminant concentrations in groundwater. A non-stationary Gaussian anamorphosis in introduced for non-linear estimation so that the estimate of the concentration is positive.<br>The method is first validated on synthetic data and then on real data from a two-dimensional cross-section of an aquifer downstream of a trench containing radioactive waste in the Chernobyl area. Kriging with the output of a simplified flow model as external drift and kriging with numerical covariances reproduce the spatial variability of the contaminant plume much better than usual (ordinary) kriging based on observations only. The comparison between the two best estimators is discussed |
| **Corresponding Author:** | Chantal de FOUQUET<br>Mines Paris - PSL<br>Fontainebleau, FRANCE |
| **Corresponding Author Secondary Information:** | |
| **Corresponding Author's Institution:** | Mines Paris - PSL |
| **Corresponding Author's Secondary Institution:** | |
| **First Author:** | Chantal de FOUQUET |
| **First Author Secondary Information:** | |
| **Order of Authors:** | Chantal de FOUQUET<br>Mathieu Le Coz<br>Xavier Freulon<br>Léa Pannecoucke |
| **Order of Authors Secondary Information:** | |
| **Author Comments:** | Fig 4 has been changed |

# Making kriging consistent with flow equations: application of kriging with numerical covariances for estimating a contamination plume

Chantal de Fouquet[1*], Mathieu Le Coz[2], Xavier Freulon[1], Léa Pannecoucke[1,2]

1. Mines Paris, PSL University, Centre for geosciences and geoengineering, 77300 Fontainebleau, France
2. Institut de Radioprotection et de Sûreté Nucléaire (IRSN), PSE-ENV/SEDRE/LELI, 92260 Fontenay-aux-Roses, France

* Corresponding author: chantal.de_fouquet@minesparis.psl.eu

**ABSTRACT**

When the data are few, kriging hydraulic head or concentration with usual variogram models can lead to physically inconsistent results, because the non-stationarity induced by the flow or transport equations is not taken into account properly. Several methods have been proposed to account for these equations in the geostatistical estimation. A recent and general approach consists of incorporating them through specific covariance models. A set of random fields sampling uncertain parameters (e.g. hydraulic conductivity) is first used as the input of a flow simulator. Empirical "numerical" spatial covariances are then calculated between pairs of points $x$ and $x'$ for the variable of interest (e.g. hydraulic head, concentration) on the corresponding set of flow simulator outputs. These non-stationary "numerical" covariances are consistent with the specific spatial variability of hydraulic head or concentrations, and they are used in the estimation. In this paper, flow-and-transport simulations are thus combined with kriging to estimate contaminant concentrations in groundwater. A non-stationary Gaussian anamorphosis in introduced for non-linear estimation so that the estimate of the concentration is positive. The method is first validated on synthetic data and then on real data from a two-dimensional cross-section of an aquifer downstream of a trench containing radioactive waste in the Chernobyl area, Ukraine. Kriging with the output of a simplified flow model as external drift and kriging with numerical covariances reproduce the spatial variability of the contaminant plume much better than usual (ordinary) kriging based on observations only. The comparison between the two best estimators is discussed.

**Keywords:** Groundwater modelling, Geostatistics, Radionuclide migration, Contamination

NOTE TO COPYEDITOR – PLEASE INSERT THE FOLLOWING AS A FIRST-PAGE FOOTNOTE

Published in the special issue “Geostatistics and hydrogeology”

## 1. Introduction

Estimating the hydraulic head or concentrations of components in groundwater is necessary for drawing a map, locating "at best" new measurements by minimalizing redundancy (Júnez-Ferreira et al., 2013), or solving the inverse problem (Gomez-Hernandez et al., 1997; Angulo et al., 1998; de Marsily et al., 2000). However the head or concentration data are generally few and the kriging estimate of these variables with a usual variogram model is not necessarily consistent with the flow physics. Various methods have been proposed to constrain estimates by flow physics, a synthesis and non-exhaustive review of which is presented here.

As the head decreases in the flow direction, it is better to carry out the kriging using a non-stationary model (Kumar, 2007). An anisotropic variogram allows one to particularize the direction of flow at the macroscopic scale. Taking covariates into account allows for improvement of the modelling. Thus, Desbarats et al. (2002) introduce the topography as an external drift of the head, choosing the appropriate support of regularization of the digital elevation model. Varouchakis et al. (2012) make a non-linear estimation of the head (using a Gaussian anamorphosis or a modified Box-Cox transformation), with the necessary correction for the back transformation of the estimated values. On a real case, the cross-validation results are improved compared to the usual kriging.

Curvilinear coordinate transformation allows for bringing back the “natural coordinates” of flow, i.e. hydraulic head and stream functions (Roth, 1995; Rivest at al., 2012). In order to explicitly introduce flow physics, Brochu et al. (2003) use the formalism of dual kriging to impose to the estimate the form of the analytical solution of a linear or radial flow calculated for a homogeneous medium. In Rivest et al. (2008) the covariate used as external drift is a « smooth » output of a finite element flow model calculated on an uniform transmissivity field, for which boundary conditions must therefore be specified. Tests on synthetic cases show that the accuracy of the estimate and its realism are improved. The method was applied to the real case of a dam.

On a synthetic case in steady state, Yang et al. (2018, 2019) reconstruct a field of concentrations by «physics-informed kriging» or «physics-informed cokriging». The method is based on a regression between observations which are considered as ”high fidelity“ data, and the average of outputs of flow and transport simulations which are considered as ”low fidelity” data. The difference between kriging and cokriging lies in the covariance of the discrepancy between low fidelity data and observations. To improve the modelling, Yang et al. (2018, 2019) suggest a non-stationary model for this discrepancy.

In another approach, covariance models are constructed so as to be approximately or accurately consistent with flow equations. In the case of steady-state linear macroscopic flow and in the absence of recharge, the linearization of the differential equation linking perturbations of head and transmissivity provides an approximated solution. Hoeksema and Kitanidis (1984) supposed the head to be stationary. Dong (1989, 1990) gave a general solution within the framework of the intrinsic

random function of order-k (IRF-k) theory and applied it to the inverse problem, by cokriging the transmissivity from transmissivity and head data. Hernandez et al. (2003) introduced a source term in the equations for performing geostatistical inversion based on the pilot points method (de Marsily, 1978; de Marsily et al., 1984). Zhang and Neuman (1996) generalized the analytical form of the simple and cross-covariance to velocity by crossing two flows with different main directions, for comparing longitudinal and transverse dispersion.

However the hypothesis of a uniform head gradient is often too strict. Roth et al. (1998) construct a variogram $\gamma(x, x')$ consistent with a steady state flow model with fixed aquifer geometry and boundary conditions. A set of geostatistical non conditional simulations of the conductivity are used as input of a flow simulation. The variogram $\gamma(x, x')$ is calculated, up to the ½ factor, as the mean square deviation of the head at pairs of points $x$ and $x$', computed on a set of flow simulation outputs. The numerical version of simple and cross-variograms (or covariances) between head and transmissivity is then used for cokriging these two variables. These experimental non-stationary variograms are used by Schwelle and Cirpka (2010) to estimate the head and the concentration by conditional expectation, calculated by the median (rather than the mean) on a set of simulations constrained by data from different variables. However, the conditional simulations of the transmissivity (or permeability) they use are obtained by an iterative inverse approach.

Pannecoucke et al. (2020) generalize the approach to the vadose zone. Non conditional simulations of saturated hydraulic conductivity are used as input to flow-and-transport simulations of a non reactive contaminant. Boundary conditions can vary between the flow simulations, if these conditions are not precisely known. Applications to a wide variety of problems are presented in Pannecoucke (2020) in two dimensions (2D) or 3D, for spatial or spatio-temporal estimation: delimitation of a contaminated zone at fixed contamination threshold and identification of the associated “uncertainty zone”, back-tracing of the unknown location of a contaminant source, comparison of the estimation with the results of a (real) 3D tracing experiment, etc.

This paper presents original results of kriging with numerical covariance, following the approach of Pannecoucke (2020), in order to take into account the heterogeneity of a contamination plume. However an anamorphosis (variable transformation) step is introduced, so that the contamination estimates are positive. This non-stationary anamorphosis is calculated on the set of the outputs of the flow-and-transport simulations. The 2D application cases refer to the highly non-stationary context of a contamination plume from a radioactive waste deposit located near the Chernobyl power station in Ukraine. A synthetic case is first examined and the estimation using real-world data is then discussed for comparing three estimation methods: usual kriging, external drift kriging with a simplified flow simulation as covariate, and kriging with numerical covariance.

## 2. Methods

### 2.1. ”Numerical” covariance

In classical kriging approaches, the covariance is inferred from observations of the variable to be estimated. However kriging is more general and can be performed based on non-stationary covariances of type $C(x, x')$. Especially, these covariances can be computed between each pair of grid nodes of the domain from a set of $N$ realizations of the variable (Pannecoucke et al., 2020), such as:

$$C(x,x') = \frac{1}{N}\sum_{n=1}^{N}\left[Z_n(x) - \overline{Z(x)}\right]\left[Z_n(x') - \overline{Z(x')}\right] \quad (1)$$

where $C(x,x')$ is the "numerical covariance" between grid nodes $x$ and $x'$ and $Z_n(x)$ (respectively $Z_n(x')$) is the value of the variable $Z$ at grid node $x$ (respectively $x'$) for the $n$-th realization. For each grid node $x$, the "numerical" covariance at all 2D grid nodes $x'$ draws a 2D map. Fig. 1 shows the maps of numerical covariances related to two different points $x$, for a set of simulated concentration plumes (see further section 3.2.). It can be shown that the numerical covariance $C(x,x')$ (or the numerical variogram $\gamma(x,x')$) has the required mathematical properties of a (discrete) covariance or variogram function (de Fouquet, 2019; Pannecoucke, 2020).

For the application (Section 3) the realizations of the variable of interest are generated by flow-and-transport simulations of a contaminant plume. First, a set of geostatistical simulations of the hydraulic conductivity is constructed and simulations of the source term of the contamination are taken from a previous work (Nguyen, 2017). The flow-and-transport simulations are based on the synthesis of several studies (Le Coz et al., 2023). Nevertheless, it should be noted that the influence of the range of the hydrogeological parameters was reduced compared with the variability between realizations and with the boundary conditions (Pannecoucke et al., 2019; Pannecoucke, 2020).

The kriging with numerical covariance can be seen as a generalization of kriging in natural flow coordinates. Indeed, a stationary covariance $K$ applied after a space transformation $f$ can be written as $K(f(x) - f(x'))$ and therefore is of the form $C(x,x')$ when the function $f$ is not linear. Conversely, in the case of a complex phenomenon, such as the development and movement of a plume, it is not necessarily the case that a space transformation $f$ and a stationary covariance $K$ exist such that the non-stationary covariance $C(x,x')$ is of the form $K(f(x) - f(x'))$. It is thus pragmatic to calculate the empirical non-stationary covariance (the "numerical covariance") on a set of outputs of the numerical flow-and-transport simulations.

### 2.2. Non-stationary Gaussian transformation

In practice, kriging with a numerical covariance does not ensure that the estimated concentration is positive. The non-linear estimation in the well-known anamorphosed Gaussian model (Chilès and Delfiner, 2012) allows avoiding negative estimates for positive quantities.

Due to the non-stationarity of the local distributions of the simulated contaminant concentrations (especially, inside vs. outside the contaminant plume), a Gaussian transformation of these distributions is performed at each grid node. The non-stationary anamorphosis $\Phi_x$ is calculated from the $N$ outputs of the flow-and-transport simulation at the grid node $x$. Thus:

$$Z_n(x) = \Phi_x[Y_n(x)] \quad (2)$$

and conversely $Y_n(x) = \phi_x^{-1}[Z_n(x)]$

where $Y_n(x)$ is the Gaussian transform of the contaminant concentration $Z_n(x)$ of the $n$-th flow-and-transport simulation at grid node $x$. Here the anamorphosis is calculated using its Hermite polynomial expansion (with 30 polynomials; Chilès and Delfiner, 2012).

The numerical covariance is then calculated on the set of the $N$ fields of Gaussian transformed variables.

The Gaussian data used for the estimation are deduced from the measurements (or from the reference data in the synthetic case) using the inverse of the anamorphosis ($\phi_x^{-1}$). The kriging estimate and the kriging variance are calculated in the Gaussian world.

Finally the conditional expectation of the concentration, its quantiles or any related functions, are calculated through the known relationship with the spatial distribution of a Gaussian random function; for example (Matheron, 1976; Chilès and Delfiner, 2012):

$$E(Z(x)|Z(x_i), i = 1, \dots, n) = \int \phi_x(Y^*(x) + \sigma(x)u)\, g(u) du \qquad (3)$$

where $E(Z(x)|Z(x_i), i = 1, \dots, n)$ is the conditional expectation of the concentration; $Y^*(x)$ is the kriging with known mean (equal to 0), $\sigma(x)$ the standard deviation of the kriging error, $g$ the density of the reduced normal distribution and $u$ is the variable to be integrated. This expression can be calculated using the formula of the Hermite-polynomial expansion of the Gaussian anamorphosis (Chilès and Delfiner, 2012). A known correction is applied on the standard deviation if the kriging with unknown mean (ordinary kriging) is used (Emery, 2006). Equation (3) ensures that the estimated concentration is positive, because the concentrations outputs of the flow-and-transport simulations used for calculating the anamorphosis are positive.

### 2.3. Estimation workflow with numerical covariances

In summary, the method involves the following steps:

- simulating a set of unconditional hydraulic conductivity fields (geostatistical unconditional simulations by any classical method, e.g. the turning bands as used here; Chilès and Delfiner, 2012);
- simulating initial source term of the contamination (geostatistical conditional simulations in the following example)
- simulating flow-and-transport on each hydraulic conductivity field to obtain a set of concentration fields;
- calculating the non-stationary anamorphosis of the concentrations at each grid node $\Phi_x$ from the set of simulated concentration fields;
- calculating the Gaussian variable for each simulated concentration field using $\Phi_x^{-1}$ ;
- calculating the numerical covariances from the set of Gaussian variables;
- calculating Gaussian data as the Gaussian transform of concentrations data using $\Phi_x^{-1}$ at data points;
- kriging of Gaussian variable from Gaussian data and computing associated kriging variance, using the numerical covariances on Gaussian transforms;

- returning to the estimated concentration (or any function of the concentration, e.g. conditional quantiles or conditional distribution) thanks to Eq. (3)

## 3. Case study

### 3.1. The trench T22 in Chernobyl

The Chernobyl accident of April 1986 released large amounts of radionuclides into the surrounding environment. In 1986 and 1987, emergency clean-up was carried out in the irradiated Red Forest, in the vicinity of the Chernobyl nuclear power plant. About $500\times10^3$ $m^3$ of contaminated topsoil, vegetation and other radioactive materials were buried in situ in hundreds of trenches dug within the permeable sandy superficial formation, directly above the water table and without engineered moisture-proof barriers (Kashparov et al., 2012).

In 1998, an experimental research facility was built around the trench T22 in order to investigate radionuclide migration processes. Then, for about 20 years, the trench T22 has been monitored extensively, allowing an advanced characterization of the site geology, the water flow regime in the unsaturated and saturated zones, the radionuclide distribution, and the speciation within and outside the trench (e.g., Bugai et al., 2012; Kashparov et al., 2012). Moreover, acquired data and knowledge were integrated into numerical models that simulate the migration of radionuclides, especially $^{90}Sr$ (Strontium-90), from the trench to the underlying aquifer (Bugai et al., 2012; Nguyen, 2017). Le Coz et al. (2023) present a detailed synthesis of previous works used for the flow-and-transport modeling near the trench.

### 3.2. Flow-and-transport simulations

Between 2000 and 2015, groundwater was collected for $^{90}Sr$ activity measurements generally once or twice a year at four sampling depths (layers L1 to L4, from top to bottom) in six wells (AP1 to AP6, from upstream to downstream) along a cross-section A-B, approximatively perpendicular to the trench T22 and assumed to be parallel to the groundwater flow lines (Fig. 2 a). A groundwater flow-and-transport model was used for simulating in 2D, i.e. along the vertical cross-section A-B (Fig. 2 b), the development of the $^{90}Sr$ plume highlighted by this monitoring (Le Coz et al., 2023). Model parameters were constant for each geological unit: eolian deposits, alluvial deposits with floodplain or channel facies (Le Coz et al., 2023). These parameters, as well as the boundary conditions, were set such that the simulated time series of $^{90}Sr$ activity were consistent with most of the measurements. This simulation with especially uniform hydraulic conductivity by geological unit is called the *calibrated simulation* hereafter.

For this study, 400 new flow-and-transport simulations are run by considering the uncertainties on the model parameters (e.g., the parameter that governs radionuclide retention on aquifer material) and boundary conditions (e.g., the percolation rate through the trench T22). In addition, for each run,

- the spatial variability of hydraulic conductivity is simulated through a random field for which the properties are determined based on textural analysis of aquifer material samples (eolian and alluvial sand). T
- the initial distribution of $^{90}Sr$ activity within the trench T22 is a geostatistical conditional simulation (Fig. 2 b) constructed from both *in situ* emission profiles and laboratory analysis of waste samples (Nguyen, 2017).

### 3.3. Spatial estimation

A set of 357 simulated fields (some simulations did not converge) of the $^{90}Sr$ activity in the saturated zone along the cross-section A-B is extracted from the flow-and-transport simulations on 1$^{st}$ October 2006 (01/10/2006). On this date, the $^{90}Sr$ activity was measured in groundwater collected at all sampling depths in wells AP1 to AP6 (Fig. 2 b). On the *calibrated* simulation, the $^{90}Sr$ plume extends up to 40 m from the trench with a downward component (Fig 3a). The geometry of the plume in the simulation set is similar, although its extent varies significantly (e.g., Fig 3b). The distribution of the $^{90}Sr$ activities computed from the simulation set at the sampling wells shows significant ranges, especially in the core of the plume (highest values) (Fig. 4), yet these ranges generally include the activity of the *calibrated simulation* and of the measurements.

Three estimation methods of the $^{90}Sr$ activity are compared in a cross-validation approach: (i) ordinary kriging (OK); (ii) kriging with an external drift (KED), the drift being the $^{90}Sr$ activity field extracted from the *calibrated simulation* (Fig. 3a); and (iii) kriging with numerical covariances (KNC) using a non-stationary Gaussian transformation, with covariances computed on the Gaussian transforms of the simulated fields of $^{90}Sr$ activity (simulations 2 to 357).

First, the simulated field 1 (Fig. 3b) is used as a synthetic case in order to compare the results with a known "reality" (this field is not considered for the covariance computation). Estimations are conditioned (i) at the wells AP1 to AP6 and then (ii) only at the most downstream well (AP6), the $^{90}Sr$ activity at the wells AP1 to AP5 being used for the assessment.

Then the actual measurements are considered. As for the synthetic case (ii) the estimations are performed only with the data belonging to the most downstream well (AP6), the $^{90}Sr$ activity at the wells AP1 to AP5 being used for the assessment.

## 4. Results

### 4.1. Synthetic case

The $^{90}Sr$ activities extracted from the simulated field 1 (i.e. the synthetic data) at the sampling locations are relatively high with respect to the activities extracted from the other simulations, included the

249 *calibrated* one (Fig. 4). At the wells, the relationship between activity "data" and covariate (*calibrated*
250 simulation) is approximately linear (Fig. 4).

251 Pragmatically, OK and KED kriging are done using an isotropic linear variogram, for avoiding the
252 variogram fitting phase under unfavorable conditions (few data and high variability). When all data at
253 the wells AP1 to AP6 are used in the estimation, the OK estimation (Fig 5a) is consistent with the
254 simulated field 1 (Fig. 3b) only close to these wells, whereas the KED and the KNC estimations (Fig. 5 b
255 and c) reproduce the geometry (extent and downward component) of the $^{90}$Sr plume on the whole
256 modeling domain. In addition, OK and KED result in negative $^{90}$Sr activity estimated values in the
257 bottom part of the domain, below the $^{90}$Sr plume. KED and KNC are similar according to the root mean
258 square error (RMSE) criterion (Tab. 1).

259 When only synthetic data at the well AP6 are used, the geometry of the $^{90}$Sr plume is still well
260 reproduced by KED and KNC but not at all by the OK (Fig. 6). KED results in negative concentrations
261 outside the $^{90}$Sr plume. The RMSE criterion calculated on all nodes (Tab. 1), or on the five validation
262 wells only, favors the KNC, and it is nearly the same for the other statistical criteria (Fig. 7 and Tab 2).

263 A scatter diagram between the estimate and “reality” (Fig. 8) confirms the good accuracy of KED and
264 KNC.

265 A test with the average of the 356 others simulations (instead of the *calibrated* simulation) as external
266 drift leads to very similar results, only slightly less precise.

267 ### 4.2. Actual measurements

268 The actual measured $^{90}$Sr activities at some sampling locations differ significantly from the activities
269 extracted from the *calibrated simulation*, but are generally (except in one location) included in the
270 range of activities extracted from the 357 additional simulations (Fig. 4). The relationship between the
271 activity at the wells and the covariate is no longer linear.

272 As for the synthetic case, when the estimations are conditioned by the actual measurements at the
273 well AP6, OK does not reproduce the lateral variability of the $^{90}$Sr activity with depth (Fig. 9a). KED
274 maintains the geometry of the $^{90}$Sr plume of the *calibrated simulation*, although the simulated activity
275 is about a half order of magnitude lower (Fig. 9b). The geometry of the $^{90}$Sr plume estimated by KNC
276 differs significantly: its extent is reduced but the $^{90}$Sr activity in its core is higher (Fig. 9c). At the five
277 validation wells, all estimates are positive. The relative performances of KED and KNC are here more
278 difficult to decide, because the “best” method varies according to the criterion (Fig. 10 and Tab. 3): the
279 mean error is smaller for KNC, the median error and the RMSE are similar for the two methods,
280 whereas the mean absolute error favors the KED. The scattered points between the estimates and
281 observations are in this case further away from the first bisector (Fig. 11). This confirms the greater
282 inaccuracy than for the synthetic case.

283 ## 5. Discussion and conclusion

284 The main processes that govern the development of a contaminant plume in groundwater can be
285 simulated using a flow-and-transport model. However, due to uncertainties in input data or
286 misrepresentation of some sub-processes, model output cannot be considered as an accurate

representation of the spatial distribution of the contaminant in groundwater at a given date. Usual kriging, e.g., ordinary kriging (OK), offers an alternative, but a high density of observations is necessary for providing realistic estimations. When observations are scarce, geostatistical approaches that take account of physically-based information, e.g., kriging with external drift (KED) or kriging with numerical covariance (KNC), are more relevant.

In KED, physically-based information consists of one or several drifts, which governs the geometry of the estimated contaminant plume. Following the literature, the output of a simplified flow model, namely with constant conductivity, is chosen here as external drift. KED requires, therefore, only one flow-and-transport simulation. In the case of actual observations, this drift is not necessarily consistent with those data; then KED could modify the variability of the estimated concentrations (location and level) of the plume.

With KNC, a set of several hundred flow-and-transport simulations are used as physically-based information for computing the numerical covariances (and optionally the non-stationary anamorphosis). On synthetic cases, when the observations are consistent with the simulation set (i.e., when observations are extracted from one reference simulation), the geometry of the contaminant plume of the reference simulation is fairly well reproduced. In the case of actual observations, the geometry of the contaminant plume could significantly differ from that of the simulated plumes. If the numerical covariance does not reflect this discrepancy, then the KNC will lead to inaccurate results. For the actual measurements of the trench T22, the estimated concentrations seem more contrasted with KNC than with KED (Fig. 9), with larger maximum values. In addition, in all cases, concentration fields estimated by KNC associated with a Gaussian anamorphosis are strictly positive.

These results corroborate the conclusions of the previous work of Pannecoucke et al. (2020), which focused on a synthetic case that represents the development of a contaminant plume in the unsaturated zone. Indeed, this study, based on a real dataset from the saturated zone, confirms that the non-stationary numerical covariances allow integrating phenomenological knowledge in the kriging estimation. Moreover, it also shows that kriging with numerical covariance could be more accurate than external drift kriging, which does not consider the uncertainties related to this covariate, especially when the geometry of the contaminant plume is complex. The quality of the estimation depends on the ability of the physically-based realizations used for computing the numerical covariances to be consistent with the actual flow-and-transport processes and the corresponding uncertainties.

However, the (unique) simplified flow-and-transport simulation used as drift for the KED requires a much lower calculation time than the set of simulations needed for computing the numerical covariances. One reviewer points out that “the workflow needed for the KNC also requires a consistent number of additional steps as compared with the other alternatives.”

Rather than a new "better method", kriging with numerical covariance appears to be an alternative to external drift kriging, which enriches the estimation methods useful to the practitioner. This general method can be applied to diverse issues in hydrogeology, in multivariate or spatio-temporal modeling, when estimating or conditioning simulations of hydraulic head or fluxes, backtracking of a plume to locate the source of a pollution (Pannecoucke, 2020), and in hydro-geochemical modelling. The method obviously applies to other contexts (e.g. air quality), and provides a very general class of covariances, e.g. on graphs or other non-Euclidean geometry.

**Acknowledgments**

The authors cordially thank the reviewers and editor whose comments greatly helped to improve the paper. Following the remarks of one reviewer, the “calibrated” simulation was used as external drift, in preference to the average of the set of simulations.

**Funding Information and Conflicts of Interest**

This study benefited from the Kri-Terres project, supported by the French National Radioactive Waste Management Agency (ANDRA) under the French “programme d’investissements d’avenir”.

The authors declare there is no conflict of interest in connection with the submitted material

**References**

Angulo J. M., Ruiz-Medina M. D. (1998) Series Expansion Approach to the Inverse Problem Journal of Applied Probability, 35(2)371- 382.

Brochu Y., Marcotte D. (2003) A Simple Approach to Account for Radial Flow and Boundary Conditions When Kriging Hydraulic Head Fields for Confined Aquifers. Mathematical Geology 35 (2) 111–139.

Bugai D., Skalskyy A., Dzhepo S., Kubko Y., Kashparov V., Van Meir N., Stammose D., Simonucci C., Martin-Garin A. (2012) Radionuclide migration at experimental polygon at Red Forest waste site in Chernobyl zone. Part 2: Hydrogeological characterization and groundwater transport modeling. J. Appl. Geochem. 27(7), 1359-1374.

Chilès J.-P., Delfiner P. (2012) Geostatistics: Modeling Spatial Uncertainty. Wiley.

Desbarats A.J. , Logan C.E., Hinton M.J., Sharpe D.R. (2002) On the kriging of water table elevations using collateral information from a digital elevation model. Journal of Hydrology, 255( 1–4) 25-38. DOI :10.1016/S0022-1694(01)00504-2.

Dong A. (1989). Kriging variables that satisfy the partial differential equation ΔZ=Y. *In* Geostatistics. Vol 1. 3rd Int. Geostat. Cong. M. Armstrong, ed. Kluwer academic publishers.

Dong A. (1990). Estimation géostatistique des phénomènes régis par des équations aux dérivées partielles (Geostatistical estimation of phenomena governed by partial differential equations). Thèse de Doctorat en Géostatistique. Ecole Nationale Supérieure des mines de Paris ; 262p.

Emery X. (2006) Ordinary multigaussian kriging for mapping conditional probabilities of soil properties. Geoderma 132(1), 75-88.

de Fouquet C. 2019. Exercices corrigés de géostatistiqu .(Geostatistical exercises with correction). Presses des mines. Paris. 320p.

Gómez-Hernández J. J., Sahuquillo J. E., Capilla A. (1997) Stochastic simulation of transmissivity fields conditional to both transmissivity and piezometric data.1. Theory. J. Hydrol 203(1–4):163–74.

Hernandez A. F., Neuman S. P., Guadagnini A., Carrera J. (2003). Conditioning mean steady state flow on hydraulic head and conductivity through geostatistical inversion. Stochastic Environmental Research and Risk Assessment 17, 329-338.

Hoeksema R.J., Kitanidis P.K. (1984) An application of the geostatistical approach to the inverse problem in two-dimensional groundwater modelling. Water Resour. Res. 20, 1003-1020.

Institut de Radioprotection et de Sûreté Nucléaire (IRSN) (2009). MELODIE Modèle d'Evaluation à LOng terme des Déchets Irradiants Enterrés. Notice théorique du code de calcul MELO version 5.0. (MELODIE Model of Evaluation at LOng term of Buried Irradiant Waste. Theoretical notice of the MELO calculation code version 5.0.)

Júnez-Ferreira H.E., Herrera G S. (2013) A geostatistical methodology for the optimal design of space-time hydraulic head monitoring networks and its application to the Valle de Querétaro aquifer. Environ. Monit. Assess. 185(4):3527-49. doi: 10.1007/s10661-012-2808-5.

Kashparov V., Yoschenko V., Levchuk S., Van Meir N. Simonucci C., Martin Garin A. (2012) Radionuclide migration in the experimental polygon of the Red Forest waste site in the Chernobyl zone - Part 1: Characterization of the waste trench, fuel particle transformation processes in soils, biogenic fluxes and effects on biota. J. Appl. Geochem. 27, 1348-1358.

Kumar V. (2007) Optimal contour mapping of groundwater levels using universal kriging—a case study, Hydrological Sciences Journal, 52:5, 1038-1050, DOI: 10.1623/hysj.52.5.1038

Le Coz M., Pannecoucke L., Saintenoy A., de Fouquet C., Freulon X., Cazala C. (2023) Do transient hydrological processes explain the variability of strontium-90 activity in groundwater downstream of a radioactive trench near Chernobyl? Journal of Environmental Radioactivity 259–260, 107101. https://doi.org/10.1016/j.jenvrad.2022.107101

de Marsily G. (1978). De l'identification des systèmes hydrogéologiques. (Identification of hydrogeological systems) PhD thesis, Univ. Pierre & Marie Curie, Paris.

de Marsily G., Lavedan G., Boucher M., Fasanino G. (1984). Interpretation of interference tests in a well field using geostatistical techniques to fit the permeability distribution in a reservoir model. In Verly G., David M., Journel A. G., Maréchal A. (eds). Geostatistics for Natural Resources Characterization, 2nd NATO Advanced Study Institute, South Lake Tahoe, CA, 1983, 831–849. D. Reidel, Hingham, MA. Pt. 2

de Marsily G., Delhomme J.-P., Coudrain-Ribstein A., Lavenue A. M. (2000) Four decades of inverse problems in hydrogeology. *In* Zhang D. and Winter C. L., eds. Modeling and Field Investigation in hydrogeology : a special volume in honor of Shlomo P. Neuman's 60th Birthday. Geological Society of America. Special Paper 348, 1-17

Matheron G. (1976) A Simple Substitute for Conditional Expectation: The Disjunctive Kriging. In: Guarascio, M., David, M., Huijbregts, C. (eds) Advanced Geostatistics in the Mining Industry. NATO Advanced Study Institutes Series, vol 24. Springer, Dordrecht.

Nguyen H.L. (2017) Contribution à la quantification des incertitudes portées par la variabilité spatiale des déchets radioactifs enterrés à Tchernobyl. (Contribution to the quantification of uncertainties caused by the spatial variability of radioactive waste buried in Chernobyl.) Thèse de doctorat. Mines ParisTech, PSL Research University.

Pannecoucke L., Le Coz M., Houzé C., Saintenoy A., Cazala C., de Fouquet C. (2019). Impact of spatial variability in hydraulic parameters on plume migration within unsaturated surficial formations. Journal of Hydrology. 574, 160-168. https://doi.org/10.1016/j.jhydrol.2019.04.016

Pannecoucke L. (2020) Combinaison de la géostatistique et des simulations à base physique – application à la caractérisation de panaches de contaminants. (Combining geostatistics and physical-based simulations – application to contaminant plume characterization) Thèse de doctorat. Mines ParisTech, PSL Research University.

Pannecoucke L., Le Coz M., Freulon X., de Fouquet C. (2020) Combining geostatistics and simulations of flow and transport to characterize contamination within the unsaturated zone. Sci. Total Environ. 699, 134216.

Rivest M., Marcotte D., Pasquier P. (2008) Hydraulic head field estimation using kriging with an external drift: A way to consider conceptual model information. J. Hydrol. 361 (3–4), 349-361.

Rivest M., Marcotte D., Pasquier P. (2012) Sparse data integration for the interpolation of concentration measurements using kriging in natural coordinates. J. Hydrol., 416-417,72-82

Roth C. (1995). Contribution de la géostatistique à la résolution du problème inverse en hydrogéologie. (Contribution of geostatistics for solving the inverse problem in hydrogeology) Doctorat en Géostatistique, Ecole nationale supérieure des mines de Paris.

Roth C., Chilès J.-P., de Fouquet C. (1998) Combining geostatistics and flow simulators to identify transmissivity. Adv. Water Resour. 21(7), 555-565.

Schwede R. L., Cirpka O. A. (2010). Interpolation of Steady-State Concentration Data by Inverse Modeling. Groundwater 48(4), 569-579.

Varouchakis E.A., Hristopoulos D.T., Karatzas G.P. (2012) Improving Kriging of Groundwater Level Data Using Non-Linear Normalizing Transformations – A field application, Hydrological Sciences, 57(7) 1404-1419. DOI: 10.1080/02626667.2012.717174, 2012.

Yang X., Tartakovsky G., Tartakovsky A. M.(2018). Physics-Informed Kriging: A Physics-Informed Gaussian Process Regression Method for Data-Model Convergence. arXiv:1809.03461v2 [stat.ML],1–24

Yang X., Barajas-Solano D., Tartakovsky G., Tartakovsky A.M. (2019) Physics-Informed Cokriging: A Gaussian-Process-Regression-Based Multifidelity Method for Data-Model Convergence. Journal of Computational Physics 395, 410-431. https://doi.org/10.1016/j.jcp.2019.06.041

435 Zhang D., Neuman S. P. (1996) Head and velocity covariance under quasi-steady-state flow and their
436 effects on advective transport. Water resources research, 32(1) 77-83

437

438

**Figure captions**

Figure 1a,b. Examples of numerical covariance maps, for two different points $x$ (red circles).

Figure 2. Views of the 3-D model of the $^{90}Sr$ inventory in 1987 in the trench T22 (computed from the mean inventory estimated by Nguyen, 2017) and locations of the wells monitored for groundwater activity. (a) Horizontal view with cumulative $^{90}Sr$ activity in depth; (b) vertical cross-section A-B .

Figure 3. Activity of $^{90}Sr$ in the saturated zone downstream of the cross-section A-B of the trench T22 simulated with the flow-and-transport model on 01/10/2006: (a) *calibrated* simulation used as external drift; and (b) simulation 1 taken as reference for the synthetic case study

Figure 4. $^{90}Sr$ activity at the sampling locations. Scatter diagram between (a) the synthetic case in abscissa (horizontal axis) and the *calibrated* simulation in ordinate (vertical axis) and (b) the actual measurements (horizontal axis) and the *calibrated* simulation in ordinate, . The grey bar represents the range of the set of 357 simulations. The black line corresponds to the first bisector.

Figure 5. Synthetic case (i.e., flow-and-transport simulation 1). Activity of $^{90}Sr$ in the saturated zone downstream of the cross-section A-B of the trench T22 (Fig. 2) estimated on 01/10/2006 conditioned at wells AP1 to AP6: (a) ordinary kriging (OK); (b) kriging with external drift (KED); and (c) kriging with numerical covariances using a non-stationary Gaussian transformation (KNC). The non-filled areas (in a and b) correspond to negative estimated activities.

Figure 6. Synthetic case. Activity of $^{90}Sr$ in the saturated zone downstream of the cross-section A-B of the trench T22 (Fig. 2) estimated on 01/10/2006 conditioned at well AP6 only: (a) ordinary kriging (OK); (b) kriging with external drift (KED); and (c) kriging with numerical covariances using a non-stationary Gaussian transformation (KNC). The non-filled area (in b) corresponds to negative estimated activities.

Figure 7. Synthetic case. Profiles of estimated activity by OK, EDK or KNC at wells AP1 to AP5, conditioned by “data” at well AP6 and “reality”. Logarithmic scale.

Figure_8. Synthetic case. Scatter diagram between estimate (abscissa) and reference value (ordinate) for the three estimation methods (OK, KED, KNC) at the five validation wells for the estimation from AP6.

Figure 9. Activity of $^{90}Sr$ in the saturated zone downstream of the cross-section A-B of the trench T22 (Fig. 2) estimated on 01/10/2006 conditioned with measurements at well AP6: (a) ordinary kriging (OK); (b) kriging with external drift (KED); and (c) kriging with numerical covariances using a non-stationary Gaussian transformation (KNC). The non-filled area (in b) corresponds to negative estimated activities.

Figure 10. Profiles of estimated activity by OK, EDK or KNC at wells AP1 to AP5, conditioned by actual measurements at well AP6, and validation measurements. Logarithmic scale.

Figure 11. Actual measurements. Scatter diagram between estimate (abscissa) and exact value (ordinate) for the three estimation methods (OK, KED, KNC) at the five validation wells for the estimation from AP6.

476 **Tables**

477 Table 1. RMSE at all 1785 grid nodes, for the two conditioning sets of wells. The very weakly negative
478 values of KED are retained. The numbers have been rounded

| Well set | OK | KED | KNC |
|---|---|---|---|
| 6 conditioning wells | 363. | 102. | 106. |
| 1 conditioning well (AP6) | 658. | 135. | 94. |

479

480

481 Table 2. Cross-validation statistics at the five validation wells (AP1 to AP5, 20 values) estimated from
482 the data of the AP6 well, for the synthetic case. Negative estimates are zeroed for the statistics of the
483 error, but their number is reported. The error is calculated as *estimate – exact data*.

| Statistic | OK | KED(0) | KNC |
|---|---|---|---|
| Mean error | -127. | -103. | 3. |
| Median error | 306. | 0. | 10. |
| Mean absolute error | 692. | 134. | 87. |
| RMSE | 908. | 227. | 135. |
| Number of negative estimates | 0 | 9 | 0 |

484

485

486 Table 3. Cross-validation statistics at the five validation wells (AP1 to AP5, 20 values) estimated from
487 the data of the AP6 well, for the actual measurements.

| Statistic | OK | KED | KNC |
|---|---|---|---|
| Mean error | -199. | -195. | -80. |
| Median error | 37. | 0. | -3. |
| Mean absolute error | 312. | 227. | 267. |
| RMSE | 589. | 472. | 477. |
| Number of negative estimates | 0 | 0 | 0 |

488

489

Figure 1

Click here to access/download;Figure;Fig1R.pdf

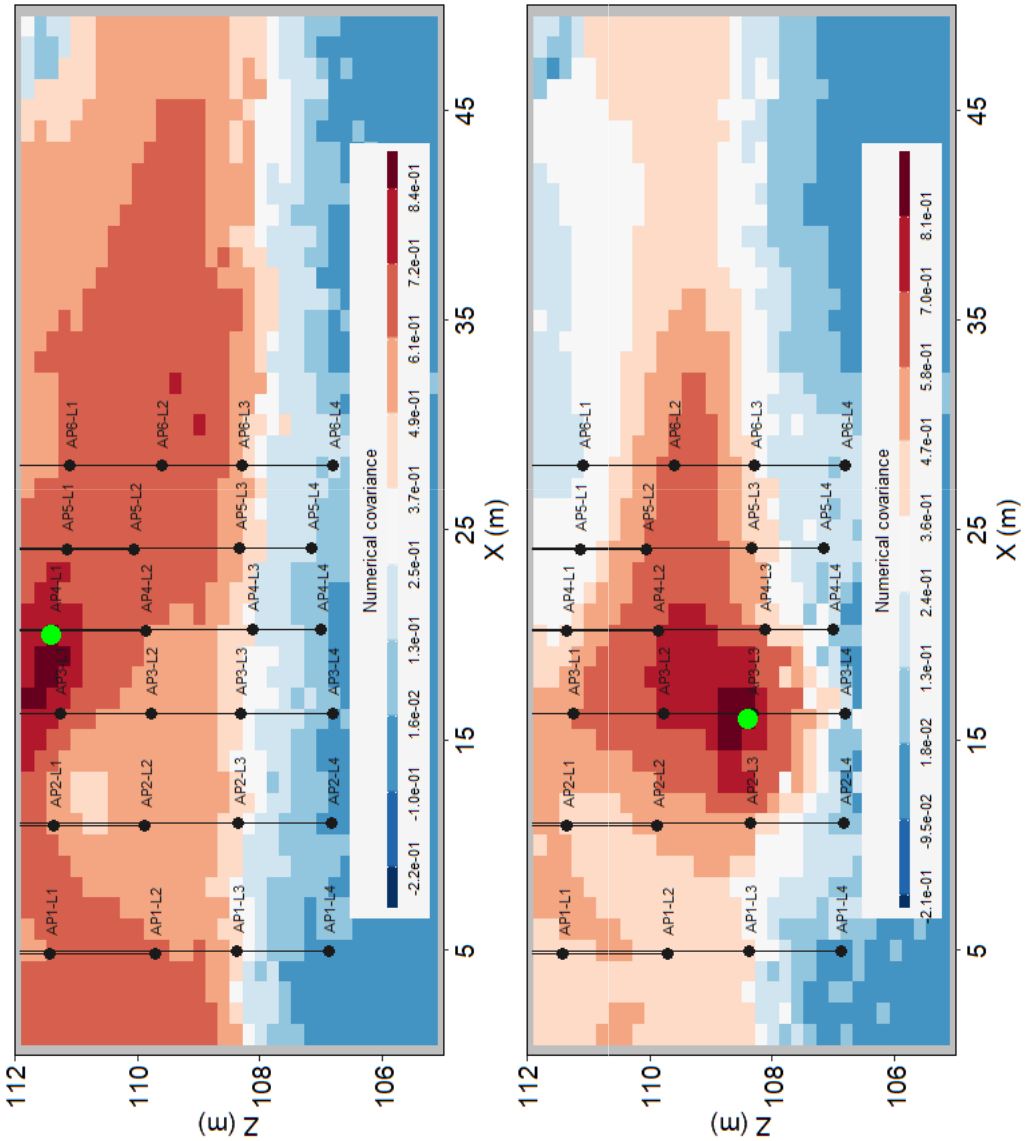

Figure 2



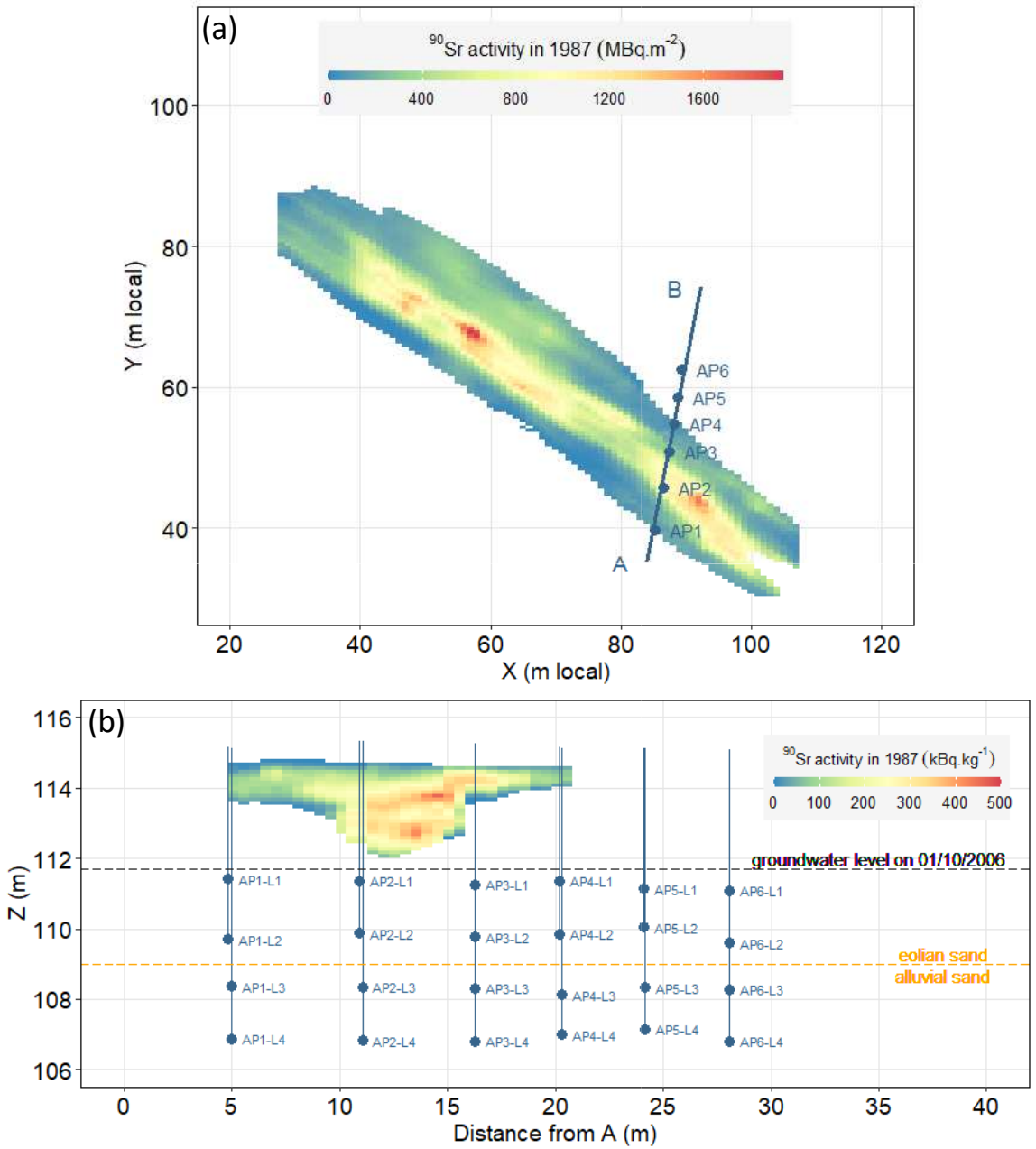

Figure 3

Click here to access/download;Figure;Fig3R.pdf

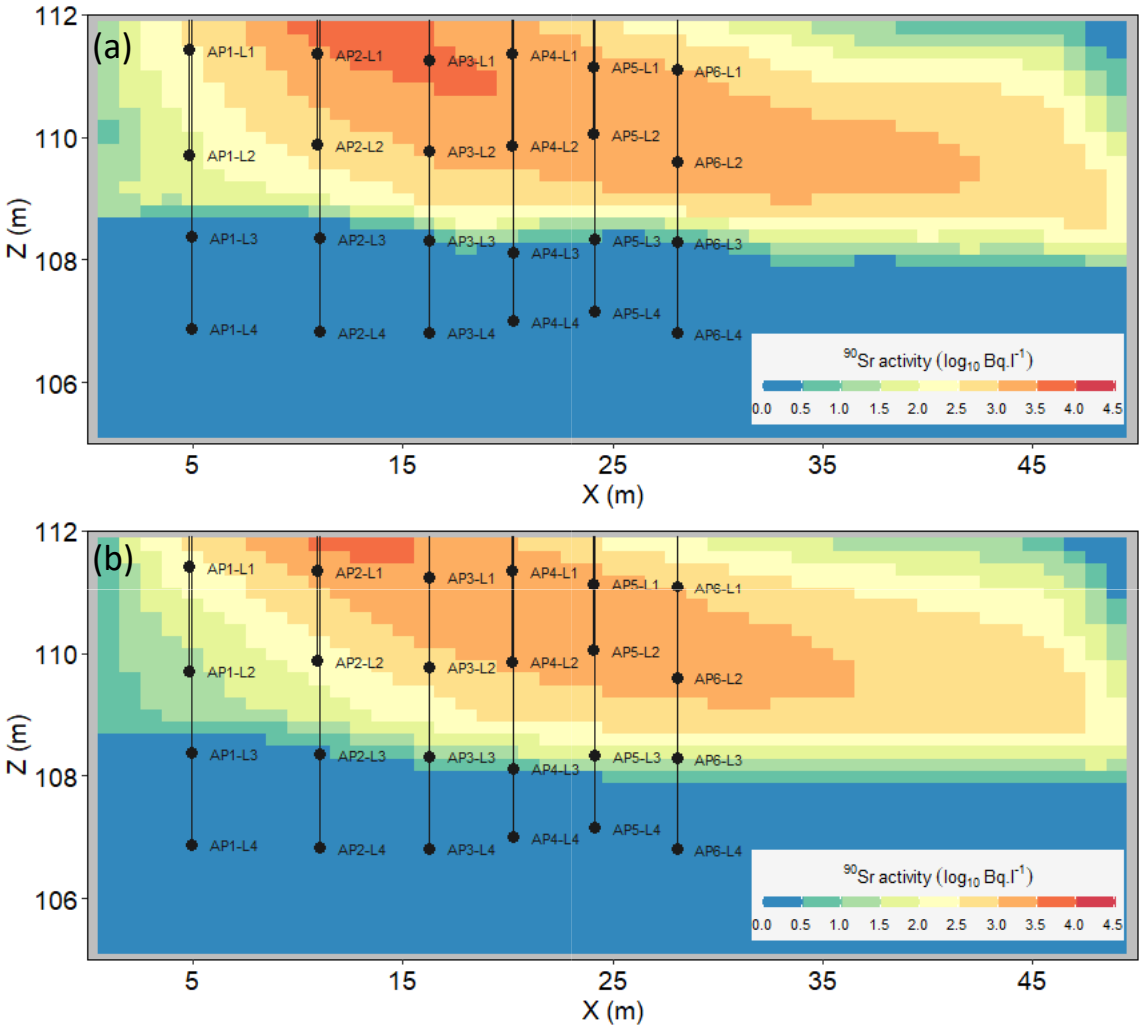

Figure 4

Click here to access/download;Figure;Fig4R.pdf

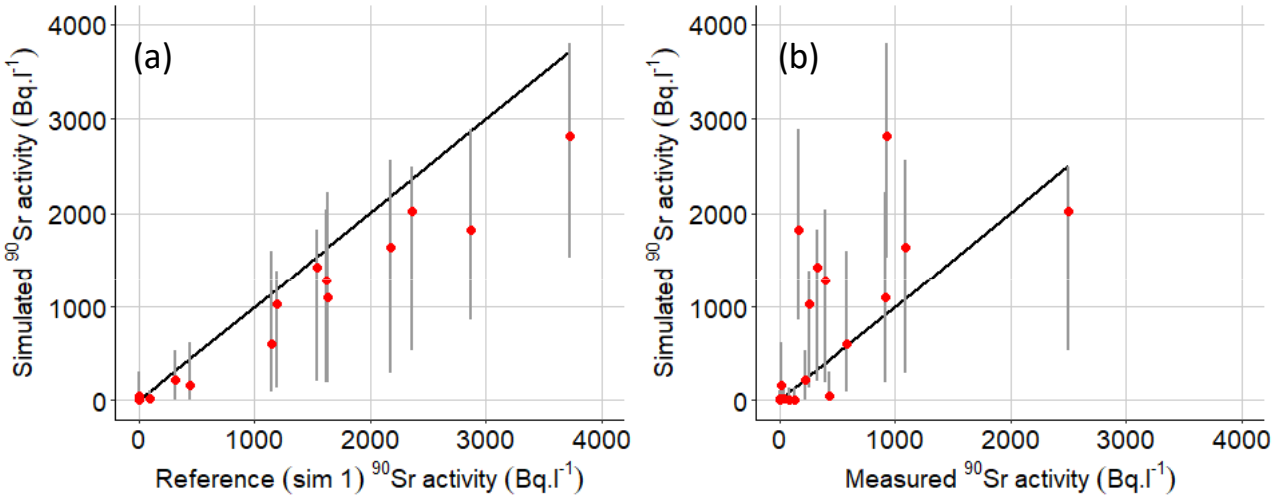

Figure 5



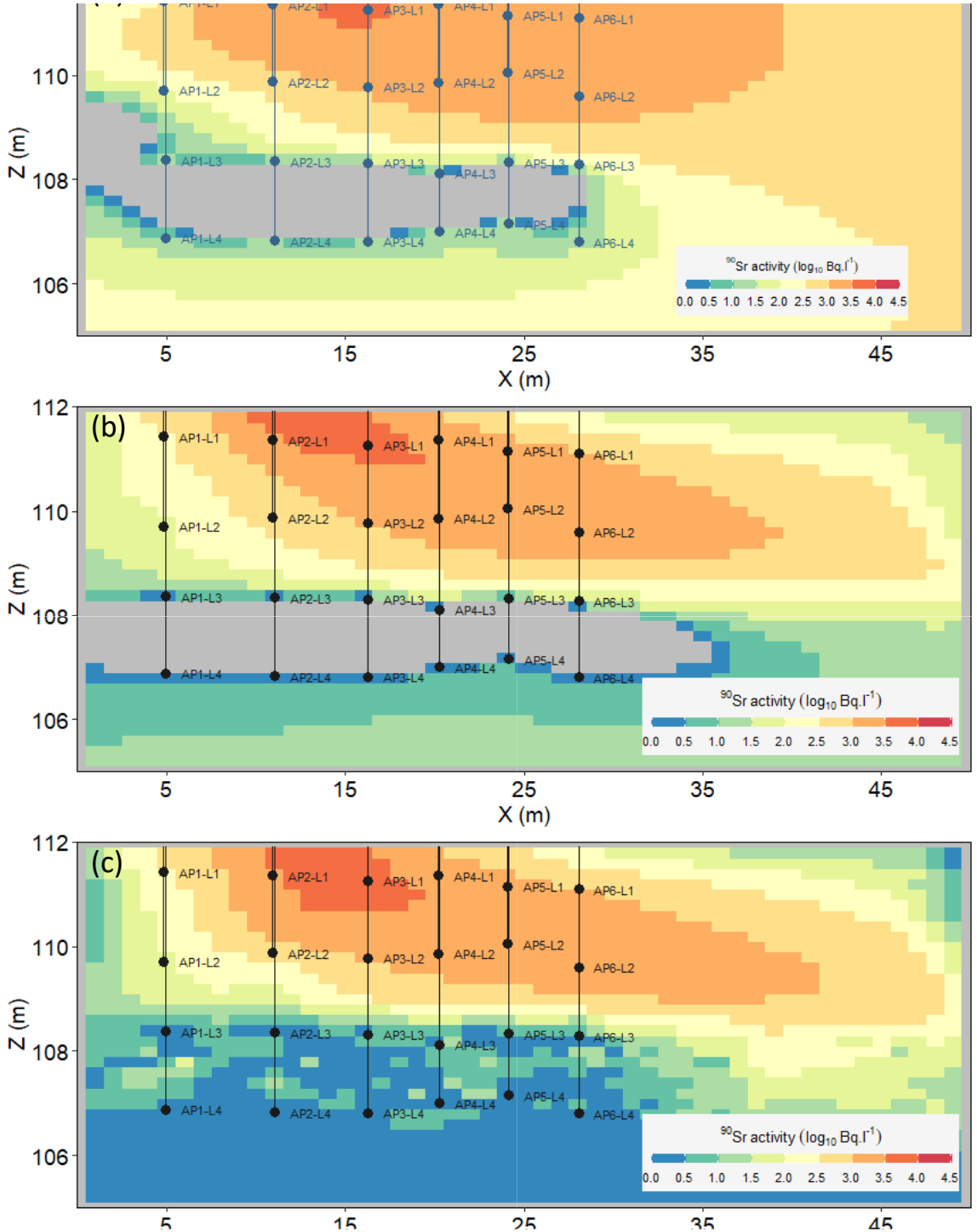

Figure 6

Click here to access/download;Figure;Fig6R.pdf

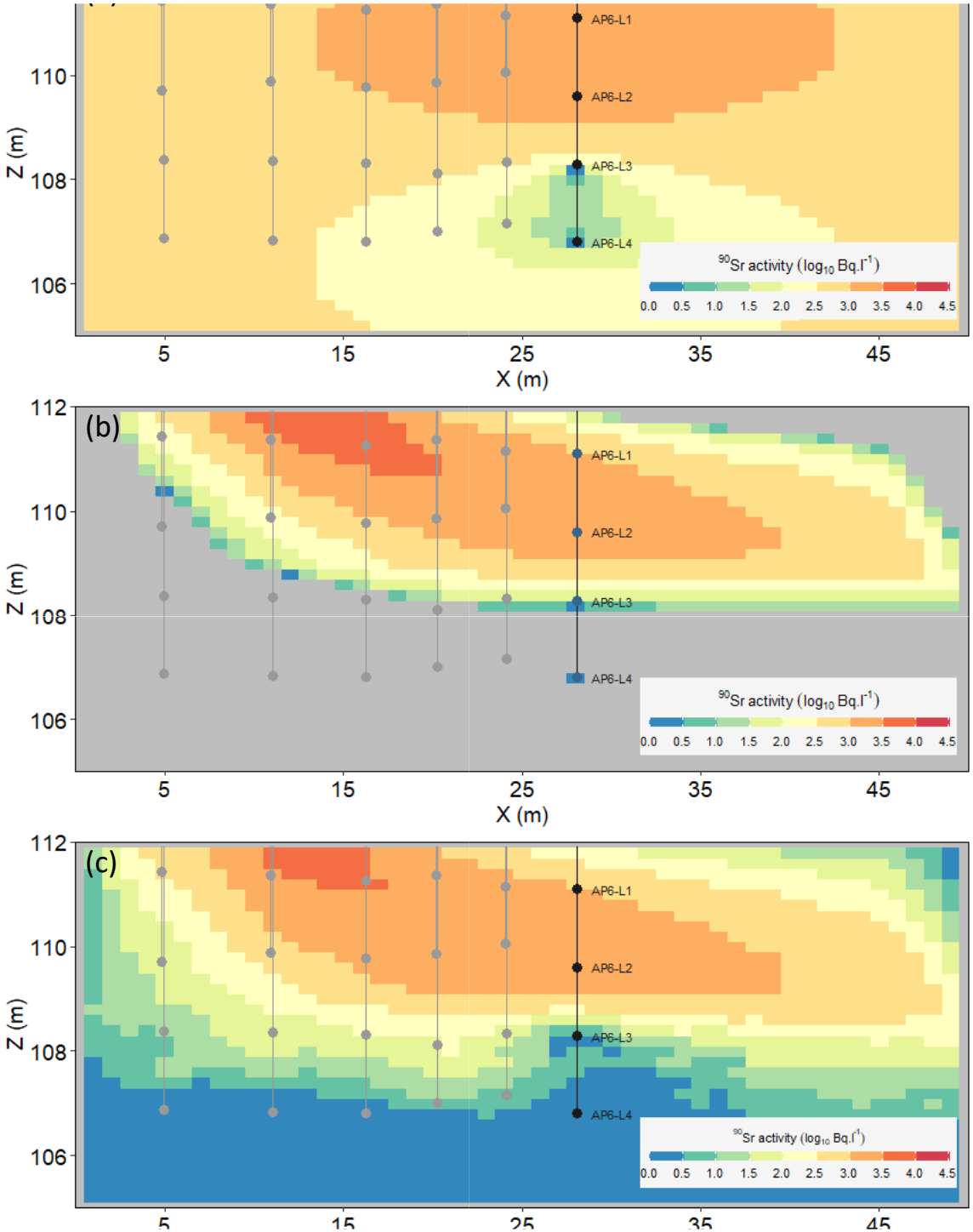

Figure 7

Click here to access/download;Figure;Fig7R.pdf

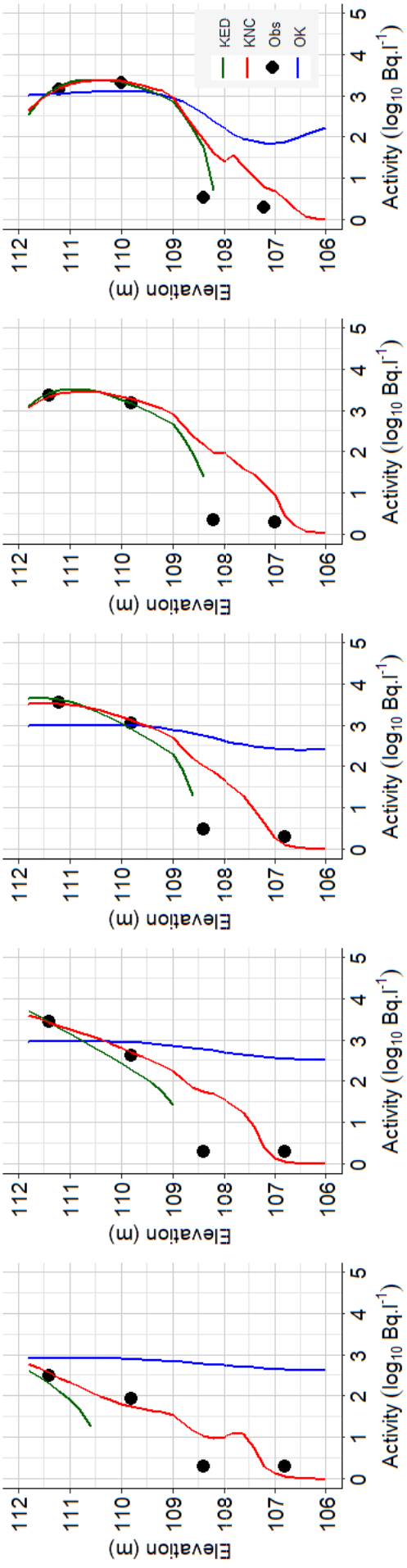

Figure 8

Click here to access/download;Figure;Fig8R.pdf

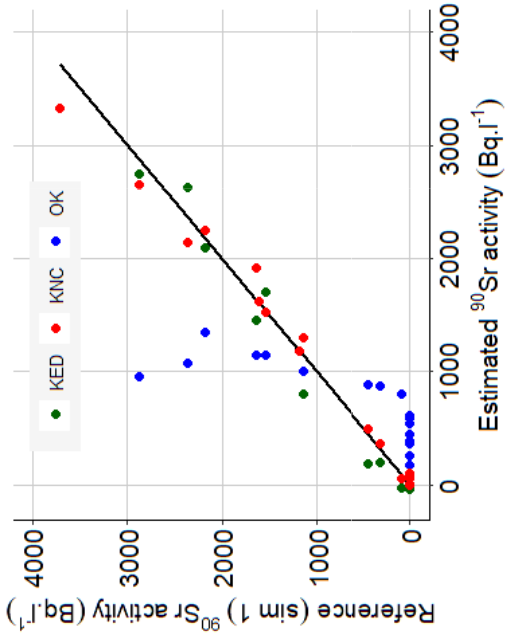

Figure 9

Click here to access/download;Figure;Fig9R.pdf

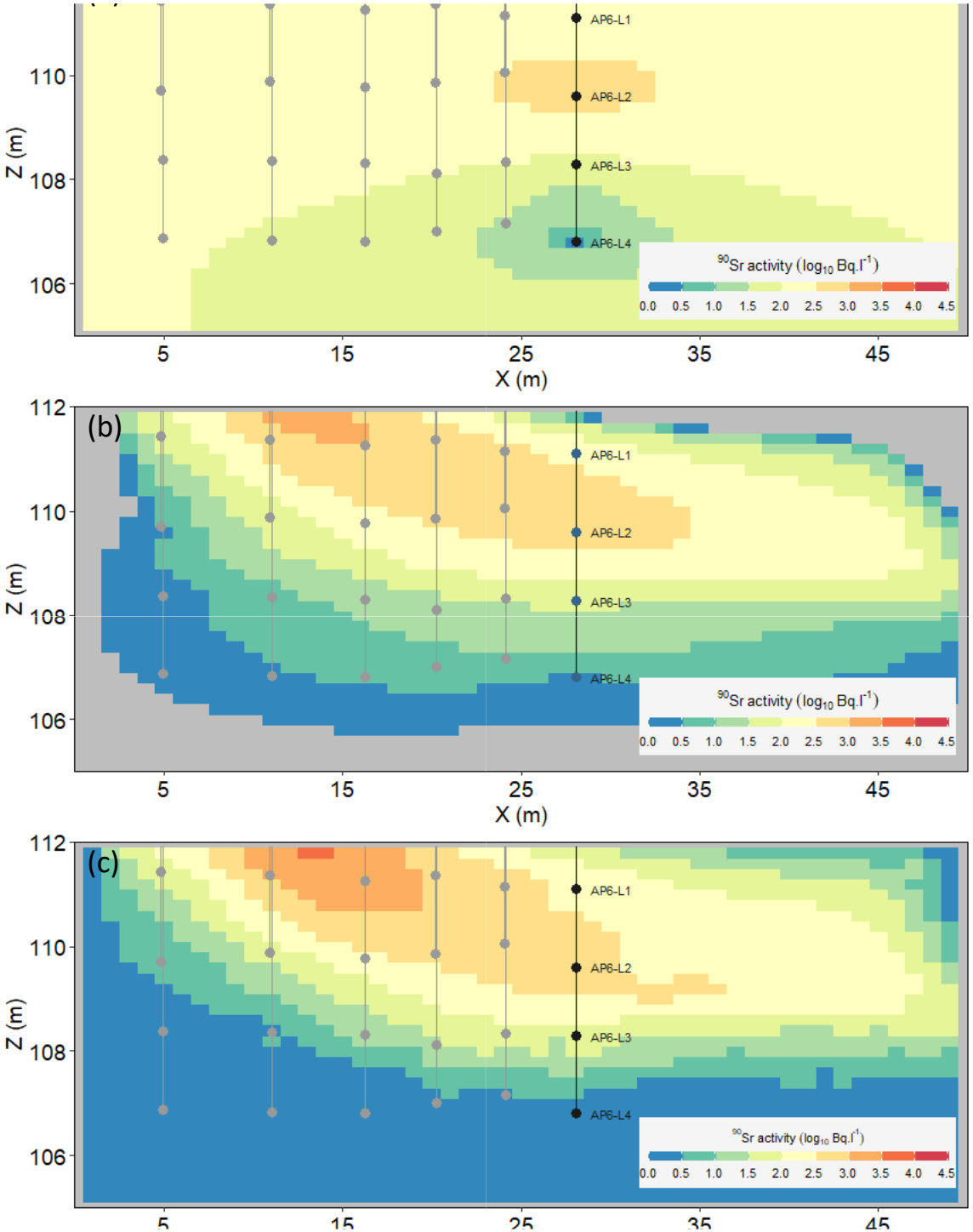

Figure 10

Click here to access/download;Figure;Fig10R.pdf

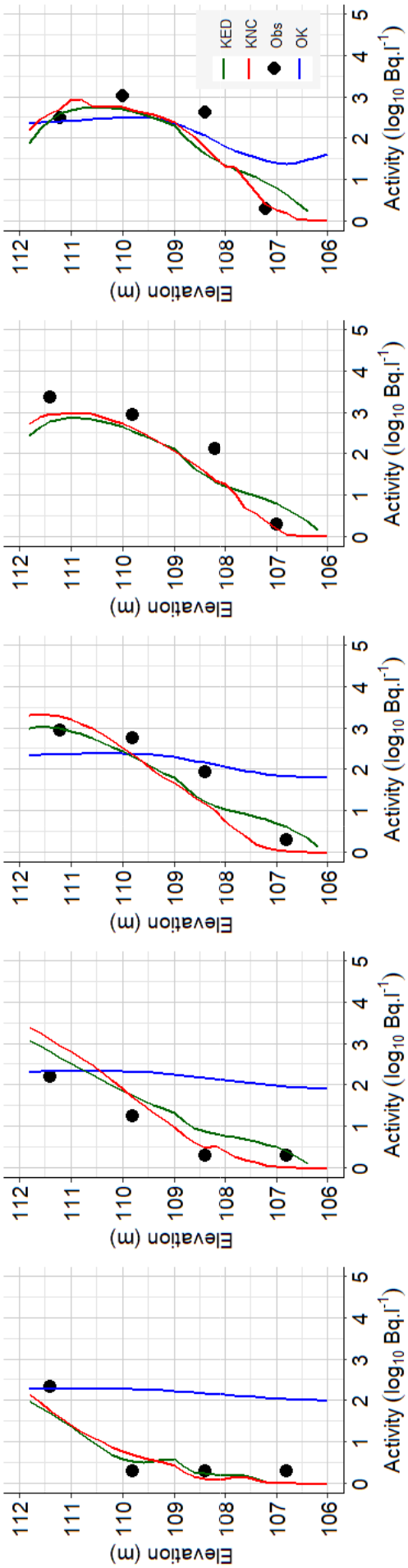

Figure 11

Click here to access/download;Figure;Fig11R.pdf

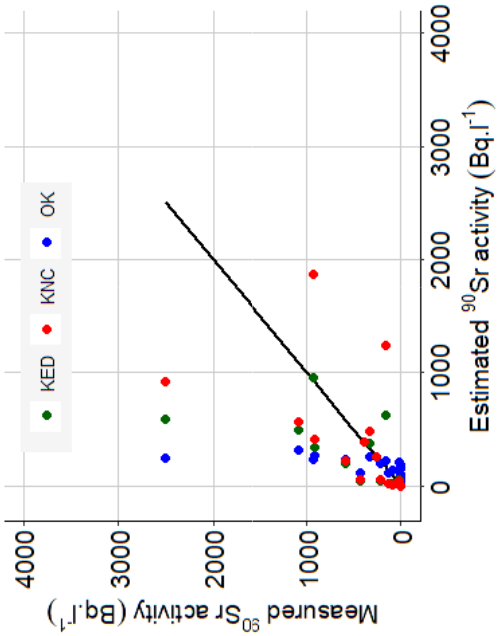

There are no comments